Journal of Materials Chemistry B

ROYAL SOCIETY OF CHEMISTRY

PAPER

View Article Online
View Journal | View Issue



Cite this: J. Mater. Chem. B, 2024, 12, 1816

# Schottky heterojunction $CeO_2$@MXene nanosheets with synergistic type I and type II PDT for anti-osteosarcoma†

Bingxin Zheng,‡[a] Ranran Zhang,‡[b] Fei Kuang,‡[c] Tiankun Hui,‡[b] Chenchen Fu,[b] Li Zhang,[d] Chuanli Zhou,[e] Meng Qiu *[b] and Bin Yue*[a]

Received 30th November 2023,
Accepted 13th January 2024

DOI: 10.1039/d3tb02835f

rsc.li/materials-b

Photodynamic therapy (PDT) has shown great potential for tumor treatment as the method is noninvasive, highly selective, and causes minimal side effects. However, conventional type II PDT, which relies on $^1O_2$, presents poor therapeutic efficacy for hypoxic tumors due to its reliance on oxygen. Here, $CeO_2/Ti_3C_2$-MXene ($CeO_2$@MXene) hybrids were successfully designed by growing $CeO_2$ *in situ* using $Ti_3C_2$-MXene (MXene) nanosheets. $CeO_2$@MXene serves as a reduction–oxidation (REDOX) center due to the presence of Ce in the lattice of $CeO_2$ nanoparticles. This REDOX center reacts with $H_2O_2$ to generate oxygen and weakens the hypoxic tumor cell environment, achieving type II PDT. At the same time, many other ROS (such as $\cdot O_2^-$ and ·OH) can be produced *via* a type I photodynamic mechanism (electron transfer process). The $CeO_2$@MXene heterojunction performs nanoenzymatic functions for synergistic type I and type II PDT, which improves cancer treatment.



## 1 Introduction

Cancer is a serious threat to human life and health and sustainable economic development. In recent years, the incidence of cancer in China has been increasing.[1] At present, traditional treatment methods, such as chemotherapy, radiotherapy and surgical resection, have been used to treat tumors, but these methods still have clinical problems, such as limited lethality to cancer cells, immunosuppression and a high recurrence rate. In recent years, the application of nanomedicine has overcome the side effects and high risks associated with traditional treatment methods,[2,3] and this method has become a development trend in clinical medical treatment. PDT has become a "new offensive weapon" to treat tumors and exhibits strong targeting properties, is minimally invasive, causes few side effects, achieves local activation and is a very promising cancer treatment.[4] PDT is a new treatment technology that involves photochemical reactions to generate toxic reactive oxygen species (ROS), which can cause damage and even death of cancer cells.[5] There are two main mechanisms in PDT treatments. One is the type II PDT treatment system, which is completely dependent on oxygen. The photosensitizer is excited by wavelength light and transfers energy to oxygen, generating singlet oxygen ($^1O_2$) to kill cancer cells. Another is the type I PDT treatment system, which involves oxygen or other molecules and the excited-state photosensitizer REDOX reaction to generate ROS (typically superoxide ions ($\cdot O_2^-$), hydroxyl radicals (·OH) or hydrogen peroxide ($H_2O_2$), breaking the REDOX balance and inducing cell death.[6] Compared with type II PDT, type I PDT can effectively produce ROS *in situ* in hypoxic tumors due to disproportionation reactions and the Harber–Weiss/Fenton reaction.[7,8]

In recent years, emerging two-dimensional (2D) materials, including graphene, have become advanced photosensitizers in the process of PDT due to their ability to absorb light at broad wavelengths, superior photoconversion performance, high ROS levels, degradability and low toxicity.[9–11] Among them, 2D transition metal carbides/nitrides show high energy absorption, flexible surface modification, good physiological stability and excellent infrared light absorption capacity.[12] MXenes effectively absorb near-infrared light in the tumor site of mice to produce photothermal effects and maintain long-term physiological stability and photostability.[13] In addition, MXenes

[a] Department of Orthopedic Oncology, The Affiliated Hospital of Qingdao University, Qingdao, Peoples Republic of China. E-mail: bonetumoryb@qdu.edu.cn
[b] Key Laboratory of Marine Chemistry Theory and Technology (Ocean University of China), Ministry of Education, Qingdao 266100, China. E-mail: mengqiu@ouc.edu.cn
[c] Qingdao University, College of Life Sciences, 308 Ningxia Road, Qingdao, Shandong Province, China
[d] Department of Operating Room, The Affiliated Hospital of Qingdao University, Qingdao, People's Republic of China
[e] Department of Spinal Surgery, The Affiliated Hospital of Qingdao University, Qingdao, People's Republic of China

† Electronic supplementary information (ESI) available. See DOI: https://doi.org/10.1039/d3tb02835f

‡ All the authors contributed equally to this work.

can be used as an ideal photosensitizer auxiliary catalyst to enhance the photocapture efficiency for PDT. For example, Jastrzebska and his collaborators found that MXene may affect the occurrence of oxidative stress and lead to the production of ROS with higher toxic effects on cancer cells compared with normal cells.[14] After the 2D molybdenum carbide prepared was used as a photosensitizer to enter tumor cells, a large amount of ROS was generated under near-infrared induction, and the solid tumor in mice was completely ablated under the synergism of photothermal stability and PDT.[15] A research group injected the MXene photosensitizer intravenously into mouse tumor cells and radiated an 808 nm laser to mouse tumor tissues for 10 min to produce a large amount of $^1O_2$, which effectively killed cancer cells and destroyed tumor tissues.[16] However, the current MXene photosensitizer involves the main mechanism that generates the type II PDT effect because the tumor microenvironment is ''congenital'' and lacks oxygen, greatly limiting the efficiency of ROS generation in the process of PDT.[17–19] To overcome the inherent contradiction between photosensitizer effects and oxygen demand, oxygen delivery or generation strategies have been used as effective solutions to compensate for the consumption of photosensitizer oxygen.[20–22]

Specific nanomaterials can also reduce $H_2O_2$ to produce more toxic ·OH.[23] A variety of nanomaterials have been reported to relieve cancer hypoxia through chemical reactions that catalyze $H_2O_2$ to produce oxygen, such as nanosized calcium dioxide[24] and nanosized manganese dioxide.[25] For example, a study prepared an integrated nanodiagnostic material based on 2D manganese dioxide and an upconversion probe. Manganese dioxide reacts with $H_2O_2$ in tumor cells to directly produce a large amount of oxygen, which greatly improves the effect of PDT.[26] Researchers improved tissue hypoxia in PDT by loading the photosensitizer chlorin to manganese dioxide and using the reaction between manganese dioxide and $H_2O_2$ to produce oxygen.[27] A team used palladium nanosheets to decompose $H_2O_2$ under near-infrared light excitation and produce a large amount of oxygen to overcome tumor hypoxia.[28] Therefore, it is effective to use tumor-responsive nanomaterials with a large oxygen supply to solve the hypoxia problem of MXene-based photosensitive materials during the photodynamic process.

Metal/semiconductor heterojunctions can further improve the photocatalytic activity by using the Schottky junction formed by metals and semiconductors and the surface plasmon resonance effect of metals; thus, these heterojunctions are a good choice for new photosensitizers.[29] For example, researchers demonstrated superior electron transport and hydroxyl radical (·OH) generation activity in silver phosphate/titanium carbide Schottky photocatalysts prepared by the electrostatic-driven self-assembly.[30] Using an *in situ* composite method, others have prepared 2D bismuth tungstate/titanium carbide Schottky heterojunction photocatalytic materials that exhibit a large interface contact area and short charge transport distance.[31] Photogenerated electrons can be transferred from a photocatalyst (bismuth tungstate) to a cocatalyst (titanium carbide) quickly and efficiently. At the same time, the photothermal effect exhibited by titanium carbide can improve the local energy to activate the photocatalyst and promote the photocatalytic reaction. Scholars prepared 2D titanium carbide/graphite phase carbon nitride heterojunction materials by the electrostatic assembly. Compared with single MXene, the separation and transfer efficiency for the photogenerated electrons of the material were significantly improved under 660 nm light, and then the generated electrons were transferred to oxygen molecules to produce superoxide radicals.[32] Therefore, utilizing MXene and 2D semiconductor materials to prepare Schottky junction photosensitized agents to achieve responsive oxygen production and reactive oxygen production in tumor hypoxia is an exploration strategy.

Regarding MXene photosensitizers in PDT against cancer tumors, the goals of this study were to address the key problems involving the lack of oxygen, prepare the $CeO_2$@MXene Schottky junction material, develop a material tumor microenvironment *in situ* with an ''inner loop'' that is responsive under continuous oxygen, perform light stimulation ''across time and space'' to generate reactive oxygen ability, and enhance the curative effect of PDT. Scheme 1 reveals the anticancer mechanism of the $CeO_2$@MXene Schottky junction intelligent response PDT system. Osteosarcoma is a rare primary malignant tumor.[33] Many studies have shown that PDT can be used to treat osteosarcoma, but its therapeutic effect is often affected by the tumor microenvironment, especially the hypoxic microenvironment.[34] Herein, a 2D cerium dioxide semiconductor and the $CeO_2$@MXene Schottky junction were prepared to address problems faced by the MXene photosensitizer in PDT. These problems involve the low therapeutic effect caused by osteosarcoma hypoxia. The material exhibits the following four characteristics: (1) the 2D heterostructure can increase the active intake of cancer cells through its high permeability and long retention. (2) after MXene and $CeO_2$ contact each other, electrons transfer to $CeO_2$, which bends the conduction band and forms Schottky junctions. Photogenerated electrons shuttle through the Schottky barrier and are enriched on the surface of MXene. The Schottky barrier prevents electrons from recombining back to $CeO_2$, which greatly reduces the charge transfer distance between materials. The surface electrons of MXene captured by $H_2O_2$ were cleaved into highly toxic ·OH, which enhanced oxygen-independent type I PDT. (3) Cerium dioxide nanosheets can react with the overexpressed $H_2O_2$ in tumor cells to produce oxygen and become a ''self-sufficient'' sustainable oxygen generator through the valence conversion of cerium ions ($Ce^{4+} \rightleftharpoons Ce^{3+}$), providing substrate supplementation and realizing ''internal circulation oxygen production'' to enhance type II PDT. (4) The amount of responsive oxygen released by ceria is intelligently regulated according to tumor activity. The more acidic the area with higher tumor activity is, the more oxygen is released and the higher the intensity of PDT. The intelligent regulation mode is realized to maximize the elimination of tumor tissues. This project will be of great practical significance for the final development of a new efficient and intelligent integrated cancer treatment system and its clinical application.

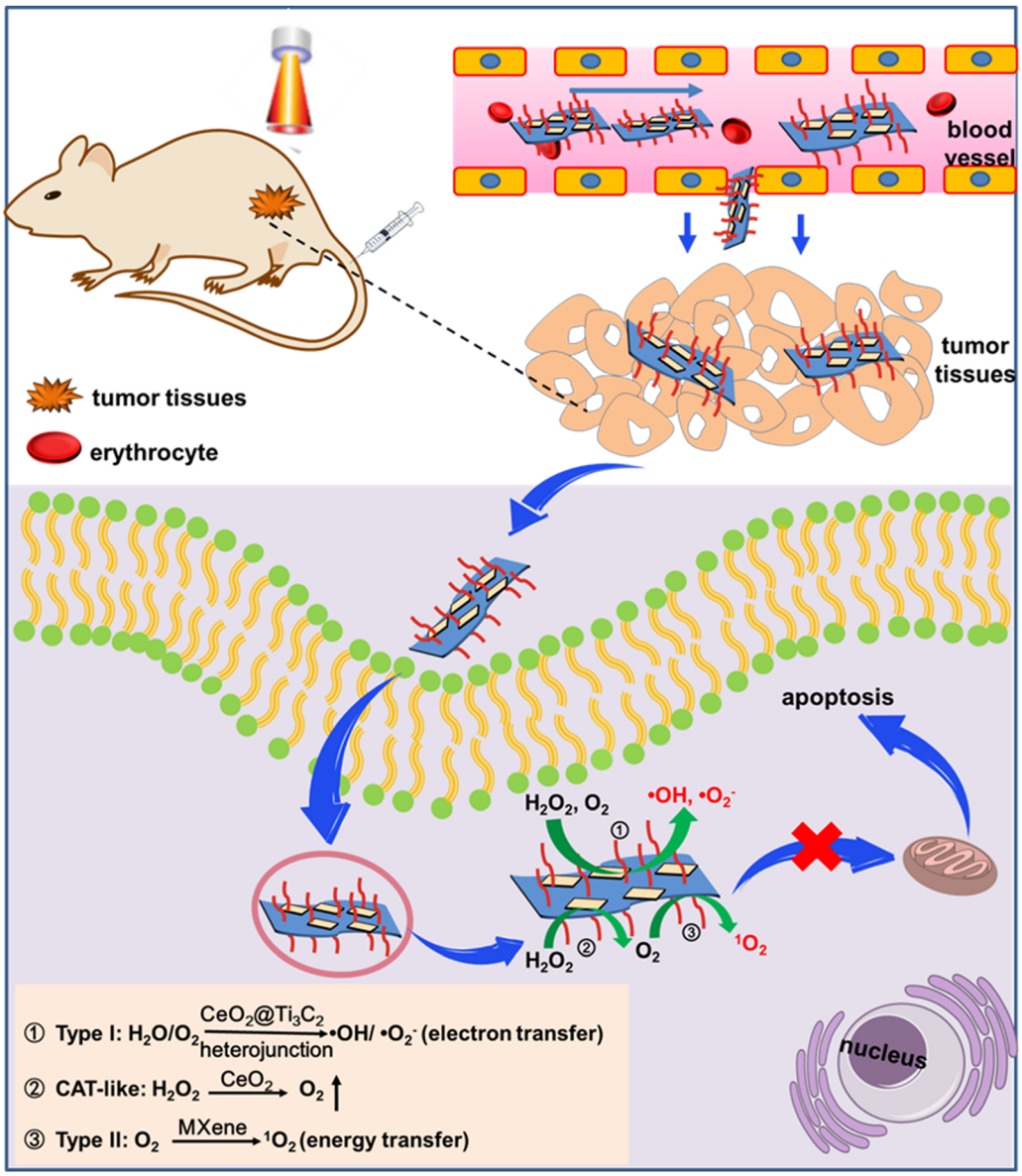


Scheme 1 Schematic diagram of anticancer photodynamic therapy based on the $CeO_2$@MXene heterojunction photosensitizer.

## 2 Experimental section

### 2.1 Instrument

The fluorescence spectra were obtained on a fluorescence spectrophotometer (F-7000, Hitachi, Japan). All fluorescence images were measured using a confocal laser scanning microscope (CLSM, FV1200, Olympus, Japan). Human 143B osteosarcoma cell tumor-bearing female BALB/c nude mice (4–5 weeks old) were obtained from Beijing Vital River Laboratory Animal Technology Co., Ltd.

### 2.2 Materials

HF (47%) was obtained from Beijing Chemical Reagents Company (Beijing, China). $Ti_3AlC_2$ (powder, 200 meshes) was purchased from Forsman Scientific (Beijing, China). MTT was obtained from Sigma-Aldrich (St. Louis, MO, USA). Dulbecco's modified Eagle's medium (DMEM), phosphate-buffered saline (PBS, pH = 7.4, 10 mM), standard fetal bovine serum (FBS), and penicillin–streptomycin were purchased from Life Technologies Corporation (Los Angeles, CA).

### 2.3 Synthesis of MXene NSs

First, the as-obtained $Ti_3AlC_2$ powder was pretreated by dispersing in 50% HF aqueous solution and stirring for 2 days at room temperature. The treated $Ti_3AlC_2$ was collected by centrifugation, washed with water and ethanol, immersed in TPAOH (tetrapropylammonium hydroxide 25 wt% aqueous solution) and stirred for another 3 days at room temperature. Finally, the MXene NSs were collected by centrifugation and washed three times with ethanol and water to remove the free TPAOH.

 

### 2.4 Synthesis of 2D $CeO_2$@MXene NSs

First, the bulk of carbon aluminum titanium was ground into powder and dispersed into hydrofluoric acid and lithium fluoride mixed solution, centrifuged, washed three times to obtain the precipitate and dispersed in the solution (*N*-methylpyrrolidone or isopropanol solution). The dispersive solution was dissected by an ultrasonic probe to prepare fewer layers of titanium carbide nanosheets. After the ultrasonic solution was processed by gradient centrifugation, MXene nanosheets with different layer distributions were prepared. Then, at 40 °C, 50 mg of MXene, 0.5 g of cerium nitrate hexahydrate and deionized water (10 mL) were mixed and stirred at high speed. The highly electronegative functional groups –OH, –F, and –O on the surface of MXene nanosheets were used to adsorb cerium ions on the surface of MXene nanosheets through electrostatic and chemical bonds. Then, 0.08 g $L^{-1}$ sodium hydroxide solution was slowly added, stirring was continued at room temperature for 0.5 h, and the mixture was transferred to a 50 mL Teflon-lined pressure reaction kettle and reacted at a certain temperature for a certain time. Through high-speed gradient centrifugation, the $CeO_2$@MXene heterojunction target material was obtained by freeze-drying to remove residual water. Additionally, mPEG-$NH_2$ was used to modify $CeO_2$@MXene NSs *via* electrostatic adsorption to obtain the $CeO_2$@MXene-PEG.

### 2.5 Photoelectric properties of the $CeO_2$@MXene Schottky junction

Transient photocurrent response and electrochemical impedance spectroscopy (EIS) were used to test the coupling of the exciton effect and built-in electric field effect between the $CeO_2$@MXene photosensitizer and the control group under 808 nm near-infrared light (power density: 1 W $cm^{-2}$) irradiation. Through the above tests, the superior characteristics of $CeO_2$@MXene photogenerated electrons were preliminarily determined, and the process used to prepare the materials was optimized through feedback.

### 2.6 Oxygen production mechanism and regulation law

The ability of $CeO_2$, MXene and $CeO_2$@MXene to release oxygen over time in the physiological aqueous solution and a simulated tumor cell microenvironment (pH = 6.5, hydrogen peroxide) was investigated to optimize the process used to prepare the materials.

### 2.7 Generation mechanism and regulation rules of ROS

The species and efficiency of ROS produced by $CeO_2$@MXene were investigated by a variety of ROS fluorescent probes under 808 nm near-infrared light (power density: 0.5–2 W $cm^{-2}$, light duration: 5–20 min) irradiation. UV-Vis and fluorescence spectra were used to detect the near-infrared excitation of the $CeO_2$@MXene solution in a three-gas incubator to simulate the normoxia (21% $O_2$, 74% $N_2$, 5% $CO_2$) of cells and hypoxia (1% $O_2$, 94% $N_2$) of tumor tissues. The yield and intensity of ROS production were observed under 5% $CO_2$.

**Singlet oxygen ($^1O_2$) detection.** The 1,3-diphenylisobenzofuran (DPBF) probe can be irreversibly oxidized by singlet oxygen to produce epoxidation compounds without visible light absorption, resulting in a decrease in the characteristic peak of DPBF at 410 nm. The effect of $^1O_2$ production was assessed through the UV-Vis detection of absorption intensity of DPBF with time. The generation efficiency was calculated, and the characteristic peak variation was observed from the spectral scanning diagram to determine the generation of singlet oxygen. To prepare the $CeO_2$@MXene composite two-dimensional material, deionized water was used to prepare a 10 mL solution with a concentration of 200 ppm. The prepared $CeO_2$@MXene, DPBF probe and hydrogen peroxide solution were placed in the sample pool to form the three concentrations in the sample pool, 20 ppm, 15 ppm and 0.1 mM, respectively. Hypoxic conditions: The nitrogen bubble solution was used for deoxygenation treatment until the content of dissolved oxygen in the solution reached below the detection limit. The sample pool was irradiated using an 808 nm laser, and the spectra were scanned every 1 min to record the characteristic peak of DPBF in the sample pool at a wavelength of 410 nm. Finally, according to the change in the characteristic absorption peak of DPBF with the extension of irradiation time, a fitting curve was created for the quantitative calculation of singlet oxygen. To ensure the accuracy and rigor of the experimental results, the characteristic absorption peak of the singlet oxygen detection probe DPBF should be controlled between 0.1 and 1. Therefore, we conducted spectral scanning for different concentrations of DPBF and determined that the optimal concentration of DPBF should be controlled at 15 ppm.

**Detection of hydroxyl radical (·OH).** The 3,3′,5,5′-tetramethylbenzidine (TMB) probe reacts with ·OH to generate ox-tmb. The time-dependent absorption peak of ox-tmb at 650 nm was measured *via* UV-VIS spectroscopy to detect the production of ·OH, and the production efficiency was calculated.

**Detection of superoxide anions ($\cdot O_2^-$).** The dihydrorhodamine 123 (DHR 123) probe can react with $\cdot O_2^-$ to generate rhodamine 123. The fluorescence emission peak of *o*-hydroxyl terephthalic acid at 525 nm was detected with time *via* fluorescence spectroscopy. Thus, the formation of ·OH was detected.

### 2.8 Cell culture

The 143B cells were cultured at 37 °C in a humidified atmosphere containing 5% $CO_2$. The medium contained 89% DMEM, 10% (v/v) FBS and 1% penicillin/streptomycin (PS).

### 2.9 Cytotoxicity measurement

The MTT assay was introduced to study the cell cytotoxicity of $CeO_2$@MXene. 143B cells were first seeded in 96-well plates at a density of $1 \times 10^4$ cells per well and cultured for 24 h. Then, the cells were treated with Opti-DMEM containing MXene/g-$C_3N_4$-TPP at different concentrations (0, 25, 50, 100, 200 and 300 μg $mL^{-1}$) and cultured for another 4 h. The media were replaced with fresh culture media and incubated for another 24 h. Then, 10 μL of 5 mg $ml^{-1}$ MTT solution was added to each well, and the cells were further incubated for 4 h. Finally, the absorbance at 492 nm of cells in each well was detected using a microplate reader to determine the cell viability.

### 2.10 Cell level study

To study the ability of 143B cells to ingest $CeO_2$@MXene, the intake of $CeO_2$@MXene in PBS (100 μg $ml^{-1}$) was studied by elemental analysis after a period of time (1–8 h). Then, the red hypoxia monitoring reagent was used to plot oxygen production during different periods of coculture with cancer cells. Third, different groups were determined using a ROS detection kit and a fluorescent probe, normal saline, $CeO_2$, MXene and $CeO_2$@MXene cocultured tumor cells with or without NIR irradiation were used to determine the amount and change in cell activity content. Through different ROS detection reagents, it was verified that the material can carry out type I and type II photodynamic mechanisms simultaneously *in vitro*, that is, corresponding to the production of hydroxyl radicals and singlet oxygen. The cytotoxicity of $CeO_2$@MXene under normoxic and hypoxic conditions was detected to verify that $CeO_2$@MXene could kill cells efficiently even under hypoxic conditions, which demonstrated that the mechanism of type I photodynamic therapy was adapted to hypoxic conditions and that the effect of type II photodynamic therapy was enhanced.

### 2.11 *In vitro* PDT

Briefly, 143B cells were cultivated in confocal dishes ($2 \times 10^5$ cells per mL) for 24 h. Then, the media were replaced with Opti-DMEM containing PBS (pH = 7.4, 10 mM), MXene-PEG (100 μg $mL^{-1}$) or $CeO_2$@MXene-PEG (100 μg $mL^{-1}$) and incubated for another 4 h. After being washed twice with PBS (pH = 7.4, 10 mM), 1 mL of fresh DMEM was added to the confocal dishes. For cell living/death evaluation, calcein-AM (1 μL) and PI (1 μL) were added to the media and incubated for 30 min to stain the cells. Then, the cells were irradiated for 5 min using an 808 nm laser (0.8 W $cm^{-2}$) or a 660 nm laser (0.48 W $cm^{-2}$), and the cells were imaged using a CLSM.

### 2.12 *In vivo* PDT

After superior oxygen production and ROS generation performance were obtained in tumor cells by data analysis, $CeO_2$@MXene with the most useful performance was selected to explore its photodynamic effect in a mouse tumor model. To establish the 143B tumor model, 100 μL of PBS (pH = 7.4, 10 mM) containing $2 \times 10^6$ 143B cells was subcutaneously injected into the right axilla of each mouse. When the tumor sizes increased to 50–80 $mm^3$ ($V$ = width$^2$ × length/2), the mice were discretionarily divided into seven therapy groups ($n$ = 5) and injected through the caudal vein with (I) PBS (pH = 7.4, 10 mM), PBS with 808 nm laser irradiation (0.8 W $cm^{-2}$) for 5 min, (II) MXene-PEG only, (IV) MXene-PEG with 808 nm laser irradiation (0.8 W $cm^{-2}$) for 5 min, and (VI) $CeO_2$@MXene-PEG and (VII) $CeO_2$@MXene-PEG with 808 nm laser irradiation (0.8 W $cm^{-2}$) for 5 min. The injection dose for each mouse was 100 μL of PBS (pH = 7.4, 10 mM) containing samples (20 mg $kg^{-1}$) or 100 μL of PBS (pH = 7.4, 10 mM). The temperature of the tumor site was recorded using an infrared thermometer. After treatment, the tumor volume and body weight of the mice were measured every five days for 3 weeks. All animals received human care and the experiments were performed according to the guidelines of the Experimental Animal Welfare Ethics Committee of Qingdao University (grant: no. 20211130BALB/c Nude3020220120091).

To study the *in vivo* intelligent photodynamic antitumor performance of the $CeO_2$@MXene heterojunction, the mouse model was divided into the following groups: group 1: PBS (pH 7.4, 10 mM), group 2: MXene, group 3: MXene + irradiation, group 4: $CeO_2$@MXene, and group 5: $CeO_2$@MXene + irradiation. The material was injected into the mice through the tail vein, the changes in tumor volume, weight, photos and survival rate of mice were recorded every other day for 20 days, and the photoresponse performance of the material in the tumor site of mice was investigated. The inhibitory effect of each group on tumor growth was compared and analyzed. At the end of the treatment, the tumor volume and survival rate of the mice were finally recorded to reveal the photodynamic anticancer effect of the materials. This study provides a theoretical and experimental basis to further confirm the potential clinical application value of MXenes.

## 3 Results and discussion

### 3.1 Synthesis and characterization of $CeO_2$@MXene

MXene nanosheets were initially obtained by etching $Ti_3AlC_2$ with hydrofluoric acid and lithium fluoride solution, and $CeO_2$@MXene composites were prepared by experimental design (Fig. 1(a)). We characterized the presence of mPEG-$NH_2$ on $CeO_2$@MXene *via* infrared spectroscopy (IR). As shown in Fig. S1 (ESI†), we could observe strong absorption peaks at 3400 nm in both spectra due to the stretching vibration of –OH. Besides, the $CeO_2$@MXene photosensitizer with modification of mPEG-$NH_2$ ($CeO_2$@MXene(PEG)) and $CeO_2$@MXene without the modification of mPEG-$NH_2$ ($CeO_2$@MXene(no PEG)) exhibited absorption peaks at 540 nm corresponding to the characteristic absorption peaks of Ce–O. And the stretching vibration peaks of –$CH_2$– and –C–O–C– were observed at 2900 nm and 1050 nm, respectively, on the IR spectrum of $CeO_2$@MXene(PEG). But none of these peaks were observed on the IR spectrum of $CeO_2$@MXene(no PEG). These results indicated that $CeO_2$@MXene was successfully modified by mPEG-$NH_2$. The low size structure of cerium dioxide and the lamellar characteristics of the $CeO_2$@MXene heterojunction were preliminarily determined *via* transmission electron microscopy. TEM images of the $CeO_2$ and $CeO_2$@MXene samples are shown in Fig. 1. The pristine $CeO_2$ exhibited a cube-like morphology with a length of 2 nm (Fig. 1(b)). In the $CeO_2$@MXene composite, cube-like $CeO_2$ was grown *in situ* on the MXene nanosheets, with the two components in intimate contact (Fig. 1(c)). Remarkably, the surface was flat and smooth.

Next, we performed the DLS experiment in different media to verify the dispersion of the materials. As shown in Fig. 1(c), the TEM image of $CeO_2$@MXene shows that the lateral size of $CeO_2$@MXene nanosheets was about 300–400 nm. The DLS (Fig. S2, ESI†) indicated the lateral sizes of $CeO_2$@MXene(PEG) and $CeO_2$@MXene(no PEG) were also around 300–400 nm in

 

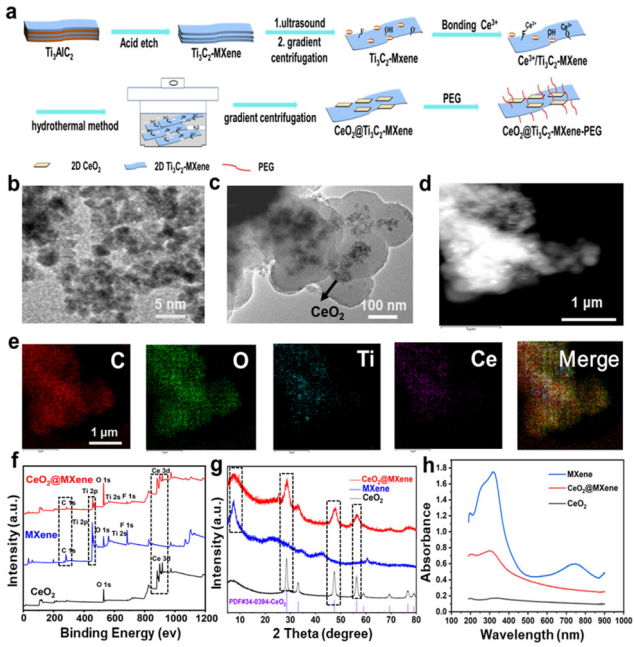


Fig. 1 (a) Schematic diagram of the preparation of the $CeO_2$@MXene heterojunction. (b) TEM image of $CeO_2$. (c) TEM image of $CeO_2$@MXene. (d) and (e) $CeO_2$@MXene-STEM images and the corresponding elemental mapping images for C, O, Ti, and Ce. (f) X-ray photoelectron spectroscopy images of $CeO_2$/MXene/$CeO_2$@MXene. (g) XRD pattern of $CeO_2$/MXene/$CeO_2$@MXene. (h) Absorption spectra of $CeO_2$/MXene/$CeO_2$@MXene.

different media. And the lateral size of $CeO_2$@MXene(PEG) nanosheets was slightly larger than that of $CeO_2$@MXene(no PEG). This result suggested that $CeO_2$@MXene has good dispersibility. In addition, we also described the dispersion property of the materials in solution through the digital images. As shown in Fig. S3 (ESI†), after standing for 24 h, MXene and $CeO_2$@MXene were well dispersed in the solution; however, $CeO_2$ was concentrated at the bottom. These results confirmed the good dispersibility of $CeO_2$@MXene in the solution. And we measured the particle size distribution of $CeO_2$@MXene(PEG) in $H_2O$, DMEM medium, saline and phosphate buffered saline (PBS) every other day for three days (Fig. S4, ESI†). We found that the $CeO_2$@MXene(PEG) nanocomposites were well dispersed in different solutions within three days. In addition, the particle diameter distribution of $CeO_2$@MXene(PEG) showed no apparent changes during these three days, which indicated that the $CeO_2$@MXene(PEG) nanocomposite has good stability. As visualized by elemental mapping images, the main elements of the $CeO_2$@MXene heterojunction, including carbon (C), oxygen (O), titanium (Ti) and cerium (Ce), were all distributed in the material (Fig. 1(d) and (e)). The EDS mapping demonstrated that the elements Ce, O, C, and Ti were homogenously distributed in the $CeO_2$@MXene sample, implying that cube-like $CeO_2$ grew uniformly on the MXene nanosheets. The coexistence of Ce, O, Ti and C in the $CeO_2$@MXene composites was confirmed *via* X-ray photoelectron spectroscopy (XPS) and X-ray diffraction (XRD). XPS spectra were collected to further corroborate the structure and chemical composition of the as-prepared samples. The survey XPS spectra of $CeO_2$ and $CeO_2$@MXene composites confirmed the existence of Ce and O in the $CeO_2$ sample and Ce, O, Ti, and C in the $CeO_2$@MXene composite (Fig. 1(f)).

In the scanning spectrum (Fig. S5, ESI†), we found that the main elements of the $CeO_2$@MXene heterojunction, including C, O, Ti and Ce, were distributed in the material. The mass fraction and atomic percentage of each element in $CeO_2$@MXene are shown in Fig. S6 (ESI†). The results were consistent with the elemental mapping images. The survey XRD spectra of $CeO_2$, MXene and the $CeO_2$@MXene composite show the crystallographic properties (Fig. 1(g)). The representative diffraction peaks of the $CeO_2$@MXene composite could be well indexed according to the typical phase of $CeO_2$ (PDF#34-0394-$CeO_2$). To ensure the accuracy of the experiment, we also tested the absorption spectra of $CeO_2$@MXene at different concentrations (Fig. S7, ESI†). Then, we found that the absorption peak was already obvious when the concentration of $CeO_2$@MXene was 20 ppm. To investigate the light harvesting capability of $CeO_2$@MXene composites, the light absorption spectra were recorded using the UV-vis diffuse reflectance spectrum measurements, as shown in Fig. 1(h). And the absorption of MXene was obvious in the near-infrared region. Meanwhile, the absorption of $CeO_2$@MXene shows a remarkable red shift due to the interaction between MXene and $CeO_2$. To a degree, this result also verified that $CeO_2$@MXene can enhance electron transfer. To determine the loading amount of $CeO_2$ in the $CeO_2$@MXene composite, we performed the inductively coupled plasma (ICP) experiment. And when $CeO_2$@MXene (no PEG) concentration was 20 ppm, the concentration of Ce was 8 ppm. The loading amount of $CeO_2$ in the $CeO_2$@MXene composite was 96.60% through calculation (w($CeO_2$)/w(MXene)).

### 3.2 Type I photodynamic therapy

In the Schottky junction photosensitizer, the presence of Ce in the lattice of $CeO_2$ nanoparticles serves as the reduction–oxidation center to react with $H_2O_2$, thus generating endogenous oxygen. Besides, the Schottky heterojunction has an internal electric field, where the electrons are excited to MXene which then react with oxygen to produce superoxide anions. Meanwhile, the excited holes of $CeO_2$ react with water to generate hydroxyl radicals for type I photodynamic therapy in the tumor microenvironment. So, the coupling of the exciton effect and built-in electric field effect of the $CeO_2$@MXene photosensitizer and control group was tested under 808 nm near-infrared light irradiation using photocurrent curves (Fig. 2(a)) and electrochemical impedance spectroscopy (Fig. 2(b)). It was determined that the presence of a strong interface effect of $CeO_2$@MXene reduced the electron transfer path and prevented photogenerated charge recombination. The photocurrent response of $CeO_2$@MXene was greatly improved compared with that of $CeO_2$ and MXene, indicating that the charge separation efficiency at the interface was greatly improved (Fig. 2(a)). Surprisingly, MXene also exhibited a relatively high photocurrent, which may result from its inherent metal-like conductivity and special layered structure. EIS measurements were conducted to investigate the interfacial charge transfer dynamics. And

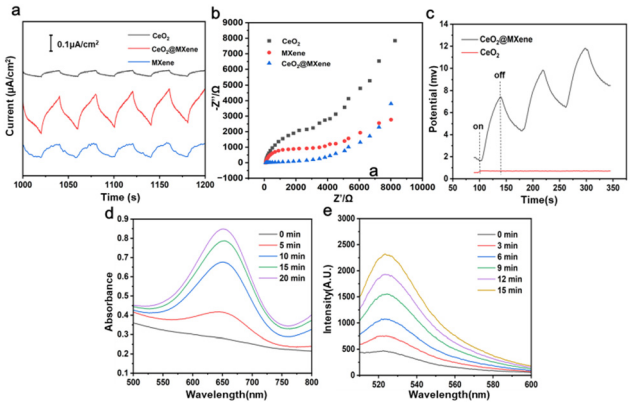


Fig. 2 (a) Photocurrent densities of $CeO_2$/MXene/$CeO_2$@MXene. (b) EIS measurement of $CeO_2$/MXene/$CeO_2$@MXene using 0.1 M $Na_2SO_4$ solution. (c) Open circuit potential measurement of $CeO_2$@MXene and $CeO_2$ in 0.1 M $Na_2SO_4$ solution. (d) Using TMB as a probe, the formation of ·OH generated by $CeO_2$@MXene was detected under different NIR irradiation time. (e) DHR 123 was used as a fluorescent probe to detect the formation of $O_2^-$ generated by $CeO_2$@MXene under different NIR irradiation time.

the lower the impedance, the higher the charge transfer efficiency.[35,36] Fig. 2(b) shows that the impedance of $CeO_2$@MXene was much smaller than that of $CeO_2$, indicating that $CeO_2$@MXene had a charge transfer resistance lower than $CeO_2$, which was beneficial to charge transfer.[37] In order to further prove that $CeO_2$@MXene has better photoelectric performance, we measured the open-circuit potential (OCP) of $CeO_2$ and $CeO_2$@MXene under light irradiation. OCP refers to the potential difference between the working electrode and the reference electrode after receiving light. The greater the potential difference, the more photo-generated carriers are generated by the photoelectric material,[38] and the higher the response signal of the external circuit. As shown in Fig. 2(c), the open circuit potential of $CeO_2$@MXene gradually increased with NIR light on and then decreased with NIR light off, indicating that the accumulation of photo-generated electrons increases the chemical potential of the surface of $CeO_2$@MXene, which further causes an increase in the open-circuit potential (OCP). In contrast, the open circuit potential of $CeO_2$ did not increase under NIR irradiation, and the open circuit potential was much smaller than $CeO_2$@MXene. This result indicated that $CeO_2$@MXene can produce more photo-generated charge carriers. In summary, through EIS and OCP, it was found that $CeO_2$@MXene has stronger photoelectric activity than $CeO_2$.

Then, the efficiency of toxic ·OH produced by $CeO_2$@MXene was investigated using 3,3′,5,5′-tetramethylbenzidine (TMB) probes under 808 nm near-infrared light irradiation (Fig. 2(d)). ·OH can cause TMB to undergo a color reaction (from colorless to blue), as shown in Fig. S8 (ESI†). It was found that with increasing irradiation time, the absorbance at 650 nm also increased, indicating that $CeO_2$@MXene can effectively produce ·OH, which can induce apoptosis of tumor cells under near-infrared irradiation. We also obtained the absorption spectra after TMB, MXene and $CeO_2$ treatments (Fig. S9–S11, ESI†). As expected, MXene and TMB did not exhibit absorption peaks at 650 nm. Surprisingly, although the absorption peak was weaker than that of $CeO_2$@MXene, the absorption peak at 650 nm appeared in the absorption spectra of $CeO_2$. This may result from the ubiquity of electron transfer in metal oxides. Then, we tested the efficiency of $\cdot O_2^-$ produced by $CeO_2$@MXene by using dihydrorhodamine 123 (DHR 123) fluorescent probes under 808 nm near-infrared light irradiation (Fig. 2(e)). Similarly, with the extension of irradiation time, the fluorescence intensity at 525 nm gradually increased. This result confirmed that $CeO_2$@MXene can produce $O_2^-$ under near-infrared light. We also obtained fluorescence spectra after DHR 123 and $CeO_2$ treatments (Fig. S12 and S13, ESI†). DHR 123 exhibited very little effect on fluorescence intensity. Similar to the absorption spectra, the characteristic peak at 525 nm after $CeO_2$ treatment was weaker than that after $CeO_2$@MXene treatment. All the results indicated that $CeO_2$@MXene was effective in the treatment of tumor tissues using type I PDT.

### 3. 3 Type II photodynamic therapy

The oxygen production of $CeO_2$@MXene and control materials detected in hydrogen peroxide (0.1 mM) was tested using a dissolved oxygen meter. The results showed that compared to single MXene and $CeO_2$, $CeO_2$@MXene generated much more oxygen (Fig. 3(a)). The composite also exhibited significantly higher oxygen productivity than that of MXene and $CeO_2$ (Fig. 3(b)). The content of dissolved oxygen in $H_2O_2$ and $H_2O$ is shown in Fig. S14 (ESI†), and some differences were observed. Therefore, we specifically tested the difference in its ability to produce oxygen in hydrogen peroxide and water (Fig. 3(c) and (d)). The absorbance in hydrogen peroxide was much less than the absorbance in water. And the ability of $CeO_2$@MXene to produce singlet oxygen in hydrogen peroxide was significantly better than that in water. Singlet oxygen yields in two different liquid environments are shown in Fig. S15 (ESI†), illustrating the same result. These results showed that the ability of $CeO_2$@MXene to produce singlet oxygen in hydrogen peroxide was significantly better than that in water.

The therapeutic mechanism of type II PDT is completely dependent on oxygen. And we have shown that endogenous $O_2$ can be continuously generated by the catalysis of Ce in the lattice of $CeO_2$ as the active site to relieve the tumor hypoxic microenvironment in the Schottky junction photosensitizer, while MXene alone can only rely on its own oxygen within the tumor cells. To further demonstrate that $CeO_2$@MXene can improve the oxygen production capacity in hydrogen peroxide and confirm that singlet oxygen was produced under hypoxic conditions, the production of singlet oxygen between $CeO_2$@MXene and MXene under normoxic and hypoxic conditions was compared. We then tested the influence of singlet oxygen generation of $CeO_2$@MXene and single MXene on DPBF absorption spectra under normoxic conditions for comparison (Fig. 3(e) and (f)). Under normoxic conditions, the ability of $CeO_2$@MXene to generate singlet oxygen was better than that of single MXene, indicating that cerium dioxide played an obvious promoting role in hydrogen peroxide. We also explored the effects of singlet oxygen generation of $CeO_2$@MXene and single

 

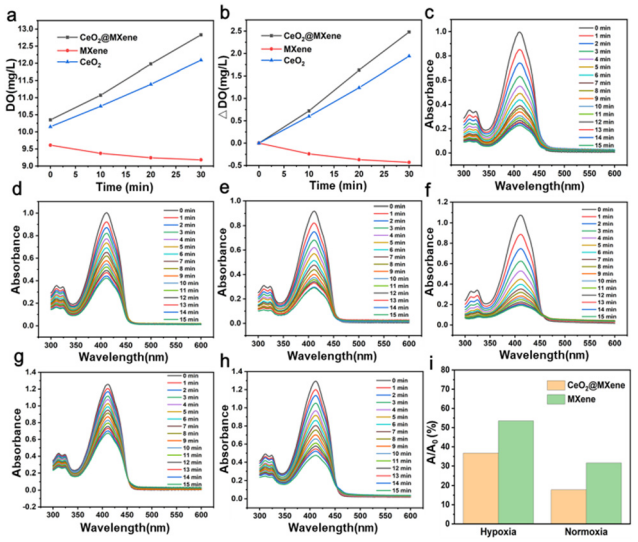


Fig. 3 Performance test of the $CeO_2$@MXene material under irradiation light (808 nm, 1.0 W $cm^{-2}$), and the test DPBF absorbance value at 410 nm wavelength: (a) Comparison of oxygen production of materials in the hydrogen peroxide solution (10 mM). (b) Comparison of the oxygen productivity of materials in the hydrogen peroxide solution (10 mM). (c) Singlet oxygen production from $CeO_2$@MXene in hydrogen peroxide. (d) Singlet oxygen formation in water from $CeO_2$@MXene. (e) Singlet oxygen production from MXene under normoxic conditions. (f) Singlet oxygen production from $CeO_2$@MXene under normoxic conditions. (g) Singlet oxygen production from MXene under hypoxic conditions. (h) Singlet oxygen production from $CeO_2$@MXene under hypoxic conditions. (i) Comparison of singlet oxygen production between $CeO_2$@MXene and MXene under normoxic and hypoxic conditions.

MXene on DPBF absorption spectra under hypoxic conditions for comparison (Fig. 3(g) and (h)). Under hypoxic conditions, the ability of $CeO_2$@MXene to produce singlet oxygen was better than that of a single MXene material in hydrogen peroxide; therefore, cerium dioxide can enhance the oxygen concentration in an aqueous solution and thus enhance the singlet oxygen production capacity. These results can be seen more clearly in Fig. 3(i). It was confirmed that cerium oxide can significantly enhance the ability of MXene to produce singlet oxygen in hydrogen peroxide, which indicates that cerium oxide can supplement oxygen and enhance the effect of type II PDT.

### 3.4 *In vitro* treatment with $CeO_2$@MXene

After verifying that $CeO_2$@MXene can induce the effect of both type I and type II PDT, we further examined the photodynamic properties of $CeO_2$@MXene, and the phototoxicity and dark toxicity of $CeO_2$@MXene were also tested (Fig. 4(a)). As the concentration of $CeO_2$@MXene increased without laser irradiation, the viability of tumor cells did not change compared with that of the control group ($CeO_2$@MXene concentration was 0). However, $CeO_2$@MXene showed significant cytotoxicity to tumor cells under laser irradiation, and cell viability decreased gradually with increasing concentration. At a concentration of 100 ppm, $CeO_2$@MXene can achieve high cytotoxicity. At the same time, we further demonstrated the cytotoxicity of $CeO_2$@MXene under hypoxic and normoxic conditions (Fig. 4(b)). As expected, under 808 nm near-infrared light, the cytotoxicity of $CeO_2$@MXene increases with increasing concentration under normoxic conditions. Surprisingly, under hypoxic conditions, $CeO_2$@MXene exhibits similar cytotoxicity under normoxic conditions. This further verified that $CeO_2$@MXene can alleviate the hypoxic conditions of tumor cells and enhance the effect of photodynamic therapy on tumor cells in the tumor microenvironment, as we had assumed.

In order to confirm the location of the internalized $CeO_2$@MXene, the intracellular trafficking of $CeO_2$@MXene was detected (Fig. S16, ESI†). The lysosome was labeled by green light and the $CeO_2$@MXene was labeled by red florescence. After treatments at different time points (0, 3, and 9 h), $CeO_2$@MXene was gradually localized in lysosome and finally escaped from the lysosome. In addition, we performed fluorescence staining experiments with living and dead cells and ROS. Tumor cell models were randomly divided into the following groups: (1) control, (2) $CeO_2$ + laser (C + L), (3) MXene + laser (M + L), (4) $CeO_2$@ MXene without laser (C–M), and (5) $CeO_2$@MXene + laser (C–M + L). As shown in Fig. 4(c), after different treatments, the control group, C + L group and C–M group showed a negligible number of dead cells, but the M + L and C–M + L groups showed a large number of dead cells. The large number of dead cells in the M + L group occurred because MXene was an ideal photosensitizer and auxiliary catalyst for photodynamic therapy. As expected, the number of dead cells in the C–M + L group was much higher than that in the M + L group, which further demonstrated that $CeO_2$@MXene can enhance the effect of photodynamic therapy on tumor cells. The result of reactive oxygen fluorescence staining in Fig. 4(d) was identical to that in Fig. 4(c), and the C–M + L group showed much higher ROS than the other groups. These results indicated that $CeO_2$@MXene exhibits a very effective inhibitory effect on tumor cells.

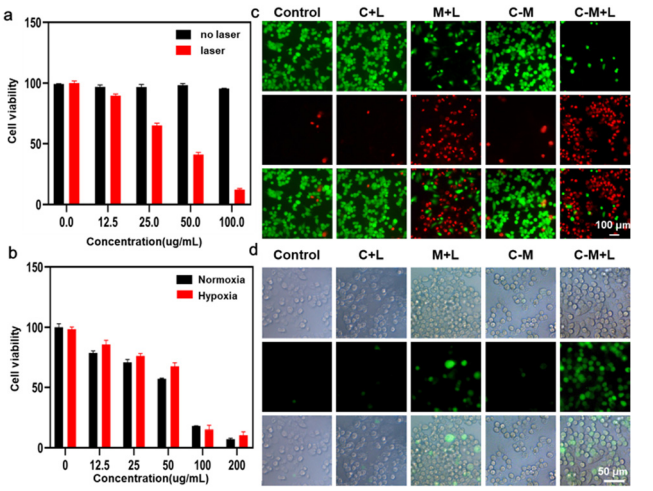


Fig. 4 (a) Light/dark toxicity of $CeO_2$@MXene. (b) Toxicity test of $CeO_2$@MXene under hypoxic and normoxic conditions. (c) Fluorescence staining of living and dead cells after different treatments. (d) Fluorescence staining of ROS after different treatments.

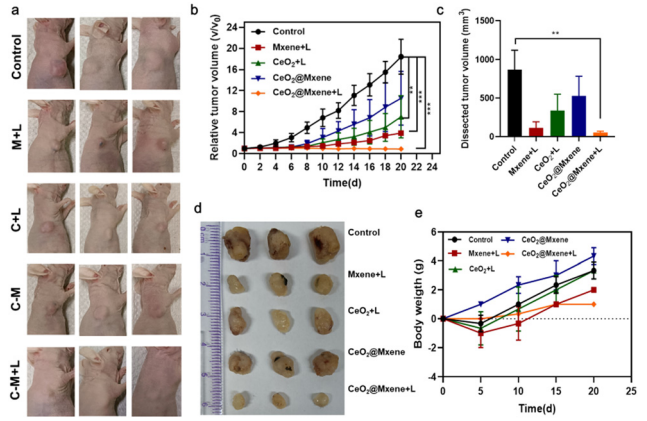


Fig. 5 (a) Whole-body digital photos of mice in each group before and after treatment. (b) Tumor volume growth curve of mice in each group during the treatment period. (c) Tumor volume of mice in each group after the end of the treatment period. (d) Digital photos of tumors of mice in each group after the end of the treatment period. (e) Body weight changes of mice in each group during the treatment period. Statistical significance was assessed by a two-tailed Student's *t* test. $*p < 0.05$, $**p < 0.01$, $***p < 0.001$. Data are expressed as mean ± S.D.

### 3.5 *In vivo* treatment with $CeO_2$@MXene

We then evaluated the efficacy of $CeO_2$@MXene *in vivo* due to its excellent photodynamic properties. The control, M + L, C + L, C–M, and C–M + L groups were designed. As shown in Fig. 5(a), the results showed that after intravenous injection, the tumor volume of tumor-bearing mice in the C–M + L group was significantly smaller than that in the other groups. In addition, the tumor volume of each treatment group was monitored every 2 days during the treatment cycle, as shown in Fig. 5(b). Compared with the control group, the tumor growth of mice in the M + L group and the C–M + L group was significantly inhibited, but the relative tumor volume of the C–M + L group was smaller than that of the M + L group. The results showed that the C–M + L group exhibited an ideal inhibitory effect on tumor growth in tumor-bearing mice. To further verify the inhibitory effect of the C–M + L group on tumor growth, tumor-bearing mice were killed after different treatments, and the remaining tumors were removed (Fig. 5(c) and (d)). The tumor volume in the C–M + L group after the end of the treatment cycle was the smallest among the treatment groups. The result also indicates that $CeO_2$@MXene exhibits stronger photodynamic properties, which can exert a better therapeutic effect on tumors. Because we must consider the biocompatibility of $CeO_2$@MXene, the body weight of tumor-bearing mice in each group was measured every 5 days after treatment began until Day 20 (Fig. 5(e)). During the treatment period, there was no significant difference in body weight between the groups compared with the control group, indicating that $CeO_2$@MXene exhibited high biocompatibility.

## 4 Conclusions

In this work, $CeO_2$@MXene heterojunctions were successfully designed by growing $CeO_2$ *in situ* using MXene nanosheets. And we successfully revealed the synergistic mechanism of $CeO_2$@MXene Schottky materials in enhancing the effect of photodynamic therapy. Compared with the existing type II photodynamic therapy method, which requires oxygen to generate singlet oxygen, the as-proposed $CeO_2$@MXene Schottky junction exhibits good biocompatibility, as a photosensitizer to realize synchronous type I and type II photodynamic therapy, and achieved good therapeutic effects. And the tumor hypoxic microenvironment could be relieved by the continuous production of intracellular $O_2$ generated by the catalysis of Ce in the lattice of $CeO_2$ as the active site to relieve. Our work lays the groundwork for developing nanomaterials with efficient oxygenation and ROS generation capabilities, thus improving the photodynamic therapy effect especially in a tumor hypoxic microenvironment.

## Conflicts of interest

There are no conflicts to declare.

## Acknowledgements

We acknowledge the financial support from the National Natural Science Foundation of China (82372478, C. Z.; 62375249, U1803128, M. Q.), the Taishan Scholar Project (tsqn201909054, M. Q.; tsqn202211362, C. Z.), the Shandong Provincial Natural Science Foundation, China (ZR2021QH038, B. Z.; ZR2021MH020, C. Z.; ZR2022JQ22, M. Q.), and the Fundamental Research Funds for the Central Universities (202341006, M. Q.).

## Notes and references

1 S. E. Kim, L. Zhang, K. Ma, M. Riegman, F. Chen, I. Ingold, M. Conrad, M. Z. Turker, M. Gao, X. Jiang, S. Monette, M. Pauliah, M. Gonen, P. Zanzonico, T. Quinn, U. Wiesner, M. S. Bradbury and M. Overholtzer, *Nat. Nanotechnol.*, 2016, **11**, 977–985.
2 Y. Shen, A. J. Shuhendler, D. Ye, J. J. Xu and H. Y. Chen, *Chem. Soc. Rev.*, 2016, **45**, 6725–6741.
3 K. Huang, J. Lin, P. Huang, G. Han and X. Chen, *Sci. Technol. Rev.*, 2018, **36**, 12–26.
4 X. Deng, Z. Shao and Y. Zhao, *Adv. Sci.*, 2021, **8**, 2002504.
5 B. D. Ravetz, A. B. Pun, E. M. Churchill, D. N. Congreve, T. Rovis and L. M. Campos, *Nature*, 2019, **565**, 343–346.
6 M. Abo, Y. Urano, K. Hanaoka, T. Terai, T. Komatsu and T. Nagano, *J. Am. Chem. Soc.*, 2011, **133**, 10629–10637.
7 T. Luo, K. Ni, A. Culbert, G. Lan, Z. Li, X. Jiang, M. Kaufmann and W. Lin, *J. Am. Chem. Soc.*, 2020, **142**, 7334–7339.
8 Z. Zhuang, J. Dai, M. Yu, J. Li, P. Shen, R. Hu, X. Lou, Z. Zhao and B. Z. Tang, *Chem. Sci.*, 2020, **11**, 3405–3417.
9 H. Wang, X. Yang, W. Shao, S. Chen, J. Xie, X. Zhang, J. Wang and Y. Xie, *J. Am. Chem. Soc.*, 2015, **137**, 11376–11382.

 

10 J. Liu, P. Du, H. Mao, L. Zhang, H. Ju and J. Lei, *Biomaterials*, 2018, **172**, 83–91.
11 M. Ma, L. Cheng, A. Zhao, H. Zhang and A. Zhang, *Photodiagn. Photodyn. Ther.*, 2020, **29**, 101640.
12 J. Shao, C. Ruan, H. Xie, P. K. Chu and X. F. Yu, *Adv. Sci.*, 2020, **7**, 2000439.
13 C. Xing, S. Chen, X. Liang, Q. Liu, M. Qu, Q. Zou, J. Li, H. Tan, L. Liu, D. Fan and H. Zhang, *ACS Appl. Mater. Interfaces*, 2018, **10**, 27631–27643.
14 A. M. Jastrzebska, A. Szuplewska, T. Wojciechowski, M. Chudy, W. Ziemkowska, L. Chlubny, A. Rozmyslowska and A. Olszyna, *J. Hazard. Mater.*, 2017, **339**, 1–8.
15 Q. Zhang, W. Huang, C. Yang, F. Wang, C. Song, Y. Gao, Y. Qiu, M. Yan, B. Yang and C. Guo, *Biomater. Sci.*, 2019, **7**, 2729–2739.
16 G. Liu, J. Zou, Q. Tang, X. Yang, Y. Zhang, Q. Zhang, W. Huang, P. Chen, J. Shao and X. Dong, *ACS Appl. Mater. Interfaces*, 2017, **9**, 40077–40086.
17 D. Chen, Z. Wang, H. Dai, X. Lv, Q. Ma, D. P. Yang, J. Shao, Z. Xu and X. Dong, *Small Methods*, 2020, **4**, 2000013.
18 L. Li, C. Shao, T. Liu, Z. Chao, H. Chen, F. Xiao, H. He, Z. Wei, Y. Zhu, H. Wang, X. Zhang, Y. Wen, B. Yang, F. He and L. Tian, *Adv. Mater.*, 2020, **32**, 2003471.
19 Y. Sheng, H. Nesbitt, B. Callan, M. A. Taylor, M. Love, A. P. McHale and J. F. Callan, *J. Controlled Release*, 2017, **264**, 333–340.
20 W. Jiang, X. Han, T. Zhang, D. Xie, H. Zhang and Y. Hu, *Adv. Healthcare Mater.*, 2020, **9**, 1901303.
21 R. Song, S. Peng, Q. Lin, M. Luo, H. Y. Chung, Y. Zhang and S. Yao, *Langmuir*, 2019, **35**, 10166–10172.
22 Y. Cheng, X. Kong, Y. Chang, Y. Feng, R. Zheng, X. Wu, K. Xu, X. Gao and H. Zhang, *Adv. Mater.*, 2020, **32**, 1908109.
23 N. Yang, W. Xiao, X. Song, W. Wang and X. Dong, *Nano-Micro Lett.*, 2020, **12**, 15.
24 Y. Xu, K. Wang, Z. Chen, R. Hu, Y. Zhao, X. Li, J. Qu and L. Liu, *Biomater. Sci.*, 2022, **11**, 119–127.
25 Y. Cheng, F. Yang, K. Zhang, Y. Zhang, Y. Cao, C. Liu, H. Lu, H. Dong and X. Zhang, *Adv. Funct. Mater.*, 2019, **29**, 1903850.
26 W. Fan, W. Bu, B. Shen, Q. He, Z. Cui, Y. Liu, X. Zheng, K. Zhao and J. Shi, *Adv. Mater.*, 2015, **27**, 4155–4161.
27 W. Zhu, Z. Dong, T. Fu, J. Liu, Q. Chen, Y. Li, R. Zhu, L. Xu and Z. Liu, *Adv. Funct. Mater.*, 2016, **26**, 5490–5498.
28 S. Li, K. Gu, H. Wang, B. Xu, H. Li, X. Shi, Z. Huang and H. Liu, *J. Am. Chem. Soc.*, 2020, **142**, 5649–5656.
29 Y. Liu, J. Guo, E. Zhu, L. Liao, S.-J. Lee, M. Ding, I. Shakir, V. Gambin, Y. Huang and X. Duan, *Nature*, 2018, **557**, 696–700.
30 T. Cai, L. Wang, Y. Liu, S. Zhang, W. Dong, H. Chen, X. Yi, J. Yuan, X. Xia, C. Liu and S. Luo, *Appl. Catal., B*, 2018, **239**, 545–554.
31 S. Cao, B. Shen, T. Tong, J. Fu and J. Yu, *Adv. Funct. Mater.*, 2018, **28**, 1800136.
32 Y. Zhang, Y. Cheng, F. Yang, Z. Yuan, W. Wei, H. Lu, H. Dong and X. Zhang, *Nano Today*, 2020, **34**, 11919.
33 M. A. Harris, M. A. Miles, T. M. Shekhar, C. Cerra, S. R. Georgy, S. D. Ryan, C. M. Cannon and C. J. Hawkins, *Cancers*, 2020, **12**, 1207.
34 Y. Wan, L. H. Fu, C. Li, J. Lin and P. Huang, *Adv. Mater.*, 2021, **33**, 2103978.
35 R. Tan, Y. Qin, M. Liu, H. Wang, R. Su, R. Xiao, J. Li, L. Hu, W. Gu and C. Zhu, *Adv. Funct. Mater.*, 2023, **33**, 2305673.
36 F. F. Xin, J.-J. Xu, J. Zhang, A.-J. Wang, Y. Xue, L.-P. Mei, P. Song and J.-J. Feng, *Biosens. Bioelectron.*, 2023, **237**, 115442.
37 E. L. Anderson and P. Buhlmann, *Anal. Chem.*, 2016, **88**, 9738–9745.
38 N. Jiang, D. Li, L. Liang, Q. Xu, L. Shao, S. B. Wang, A. Chen and J. Wang, *Nano Res.*, 2020, **13**, 1354–1362.